Materials Advances

ROYAL SOCIETY OF CHEMISTRY

PAPER

View Article Online
View Journal | View Issue

Cite this: *Mater. Adv.*, 2022, 3, 5930

Enhancing the third-order nonlinearity and crystallinity by selenium incorporation in tin sulfide films ($SnS_{1-x}Se_x$) for optoelectronic applications

Abinash Parida,[a] D. Sahoo,[a] D. Alagarasan,*[b] S. Vardhrajaperumal,[c] R. Ganesan[b] and R. Naik *[a]

Thin films of $SnS_{1-x}Se_x$ with varying Se (x = 0, 0.1, 0.15, 0.2, 0.25) contents were deposited by the thermal evaporation method on glass substrates at room temperature. The crystalline nature of the films is verified using structural characterization techniques such as X-ray diffraction and Raman analysis. The crystallinity increased with Se concentration. The nanoflake-like structure with an increase in size and density upon Se addition is observed from the morphology study through field emission scanning electron microscopy. The energy-dispersive X-ray analysis confirmed the elemental % in different films. The transmittance data were recorded in the range of 900–1100 nm by UV-Vis spectroscopy and used to evaluate the linear/nonlinear optical properties. The transmission percentage decreased with the doping of Se in the SnS binary compound. The absorption and extinction coefficients were enhanced with Se content. The bandgap value decreased with the doping concentration. The optical energy gap is used to evaluate the static refractive index using Dimitrov and Sakka's relation. The value of the static refractive index increased with Se content, which further helped to enhance the nonlinear optical parameters. The nonlinear parameters such as the nonlinear refractive index and third-order nonlinear susceptibility increased with the Se concentration. The theoretically calculated physical parameters like the average heat of atomization decreased with Se content. Tuning of nonlinear and linear properties by varying the selenium doping content in $SnS_{1-x}Se_x$ films will be useful in many photonic and optoelectronic devices.

Received 29th April 2022,
Accepted 3rd June 2022

DOI: 10.1039/d2ma00485b

rsc.li/materials-advances

1. Introduction

Recently, scientists have focused on non-toxic, low-cost semiconductor materials to improve the absorber layers used in photosensing devices. Typically, materials like metal chalcogenides,[1] monochalcogenides,[2] graphene,[3] and phosphorene[4] have inherent applications in the fields of photovoltaics and optoelectronics. Among them, metal chalcogenides are widely used materials having the most favourable semiconducting properties with a low bandgap for application in advanced electronics and photonic devices.[5] Among metal chalcogenides, tin chalcogenide semiconductors have potential applications in thermoelectric devices, optoelectronics, memory switching devices,[6] photovoltaics, lithium-ion batteries,[7] and photocatalysts.[8] Tin chalcogenides are favourable candidates to be used in high-performance photodetectors for their exceptional absorption coefficient, carrier mobility, and suitable bandgap (0.81–2.31 eV).[9,10] Recently, these materials have attracted more attention due to their non-toxic, low-cost, and abundant nature.[11] Layered tin chalcogenides also exhibit excellent anisotropic properties. Previously reported tin chalcogenides like SnSe and SnS possess anisotropic electrical conductivity due to the difference in the electronic masses of electrons and holes along the axes.[12] SnS compounds exhibit layered orthorhombic structures with favorable direct and indirect bandgap values of 1.2 to 1.7 eV and 1 to 1.1 eV, respectively, for potential applications in photovoltaic cells.[13] Tin sulphide has favorable properties like p-type electrical conductivity, an orthorhombic crystal structure, and a significant absorption coefficient for making absorber layers in the preparation of thin-film heterojunction solar cells.[14,15] The constituent atoms Sn and S are tightly bonded by weak van der Waals forces and form a chemically inert surface without any surface dangling bonds and density of states, thus increasing the transparency and making the surface chemically and environmentally stable.[16] SnS and SnSe compounds

[a] *Department of Engineering and Materials Physics, ICT-IOC Bhubaneswar, 751013, India. E-mail: ramakanta.naik@gmail.com*
[b] *Department of Physics, Indian Institute of Science, Bangalore, 560012, India*
[c] *Centre for Nano Science and Engineering, Indian Institute of Science, Bangalore, 560012, India*

have been studied on a large scale by using various synthesis methods, such as chemical/physical vapor deposition,[17,18] sputtering, solvothermal,[19] and pulsed laser deposition.[20] The photodetectors made from the compounds of SnSe and SnS exhibit large values of responsivity (10^2–10^4 A W^{-1}) and average external quantum efficiencies (EQEs). For the improvement of SnSe- and SnS-based photodetectors, several approaches like alloy engineering and van der Waals heterostructures are adopted. Xia *et al.* have reported the use of a combination of both alloy engineering and van der Waals heterostructures for the SnS–SnS_xSe_{1-x} core–shell structure.[21] Alloy engineering effectively enhances the photodetection properties and tunes the semiconductor's band structure and carrier types. Recently, different techniques such as doping and annealing were used to control the carrier concentration and conductivity of tin sulphide to improve the performance of SnS based solar cells. Doping of some metal elements like Sb, Bi, Cu,[22] Ag,[23] In,[24] and Se[25] has been reported for enhancing the properties of SnS.[26,27] The hole concentration is increased by doping of Se into SnS. Yu *et al.* have reported that Se doping into the SnS host matrix increases the photoconductivity, hole concentration, and conversion efficiency and reduces the optical bandgap.[28] This suggests that Se doped SnS has more potential optoelectronic applications than pure SnS. The $SnS_{1-x}Se_x$ matrix involves higher charge carrier transport phenomena than SnS, with a decrease of the S content.[29,30] Thus, it is possible to improve both the electronic and optoelectronic properties of the as-prepared SnS and SnSe crystals by the alloying technique. Furthermore, the Sn–S–Se matrix exhibits an energy gap value in the order of the optimum energy gap for solar cells and a large absorbance near the infrared region, making it a suitable material for solar cells and optoelectronic applications.[31,32] Moreover, for the $SnS_{0.5}Se_{0.5}$ system, the on/off ratio can be enhanced up to 2.10×10^2 at room temperature, which is two times larger than those of SnS and SnSe.[29] In view of many optoelectronic properties and potential futuristic applications, we have synthesized and investigated the properties of Se doped SnS, *i.e.* $SnS_{1-x}Se_x$ (x = 0.1, 0.15, 0.2, 0.25).

In this study, nanostructured SnS and Se doped SnS bulk alloys were prepared by the melt quenching method, and the corresponding films were coated on glass substrates by the thermal evaporation process. The influence of the Se content in SnS on optical and structural properties was studied through different experiments. The present work aims to explore the tuning of nonlinear/linear optical properties like the nonlinear refractive index, third-order optical susceptibility, refractive index, optical bandgap, *etc.* in $SnS_{1-x}Se_x$ thin films at different selenium concentrations. The phase formation and crystallinity were analyzed by X-ray diffraction (XRD) and Raman spectroscopy. The energy dispersive X-ray (EDX) analysis was used for compositional analysis, and field emission scanning electron microscopy (FESEM) was used to analyze the surface morphology changes. The nonlinear/linear optical parameters of Se doped and undoped SnS thin films were calculated from the UV-visible spectroscopy data. The theoretical physical parameters like the heat of atomization, average coordination number, and bond strength were calculated and well discussed.

2. Experimental work

2.1. Preparation of thin films

The bulk $SnS_{1-x}Se_x$ (x = 0, 0.1, 0.15, 0.2, 0.25) samples were prepared by the melt quenching process. The high purity (99.999% Sigma-Aldrich) elements of Sn, Se, and S were used to prepare the bulk sample. Stoichiometric amounts of constituent elements were sealed in an evacuated quartz ampoule at a 10^{-5} torr vacuum. The quartz ampoule was placed in a furnace, and the temperature was maintained at 900 °C for 24 h with at a rate of 3 °C to 4 °C per minute. After 24 h of melting, the ampoule was removed and immediately placed in a cold water bath to avoid crystallization. The obtained bulk sample was ground to powder form and used to prepare the thin film. The thin film was deposited on a Corning glass substrate by the thermal evaporation technique using a HINDI-HIVAC Model 12A4D vacuum coating unit under a vacuum of 10^{-5} torr. The films were coated at a rate of 0.5 nm s^{-1} to a thickness of ~800 nm which was measured using a thickness monitor.

2.2. Characterization methods

The structural analysis of $SnS_{1-x}Se_x$ films was done with a Bruker D8 Advance X-ray diffractometer with a copper target used as the X-ray source. The source has a wavelength of 0.154 nm. The X-ray spectra were recorded in the scan range of 10° to 80° at a scanning speed of 1° min^{-1} and a step size of 0.02° s^{-1}. The surface morphology was examined using a Carl Zeiss Ultra 55 FESEM unit. An EDX system was used to analyze the elemental compositions. Surface scans were taken with a sample size of 1 × 1 cm^2 at 3–4 positions at 20 kV and 40 mA emission current with a pressure of 2×10^{-7} torr. Raman data were recorded using a LabRAM HR system in the range of 100–400 cm^{-1} by using an argon laser source and a backscattered CCD detector. A Bruker Optics IFS66v/S UV-visible spectrometer was used to record the optical transmission and absorption spectra in the visible range.

3. Results analysis and discussion

3.1. XRD study

The XRD pattern of $SnS_{1-x}Se_x$ nanoflakes with different Se doping concentrations (x = 0, 0.1, 0.15, 0.2, 0.25) is shown in Fig. 1(a), which reveals the crystalline nature of all the samples. The diffraction peaks of all the samples matched well with the International Center for Diffraction Data (ICDD). From the analysis, it is observed that the crystalline peaks belong to the orthorhombic phase of tin sulphide, having the reference code ICDD PDF No. 00-39-0354. From the X-ray diffraction spectra, the prominent peak at $2\theta \sim 31.68°$ is due to the reflection of the (1 1 1) plane which has the largest spacing in orthorhombic tin sulphide. The peak intensity of crystalline phases increased with the increase of Se doping, indicating an increase in crystallinity. From the X-ray diffraction analysis, there is no phase change and no additional peaks are obtained in the SnS phase. But the crystalline peaks shifted towards the lower angle side due to the expansion of lattice parameters with an increase

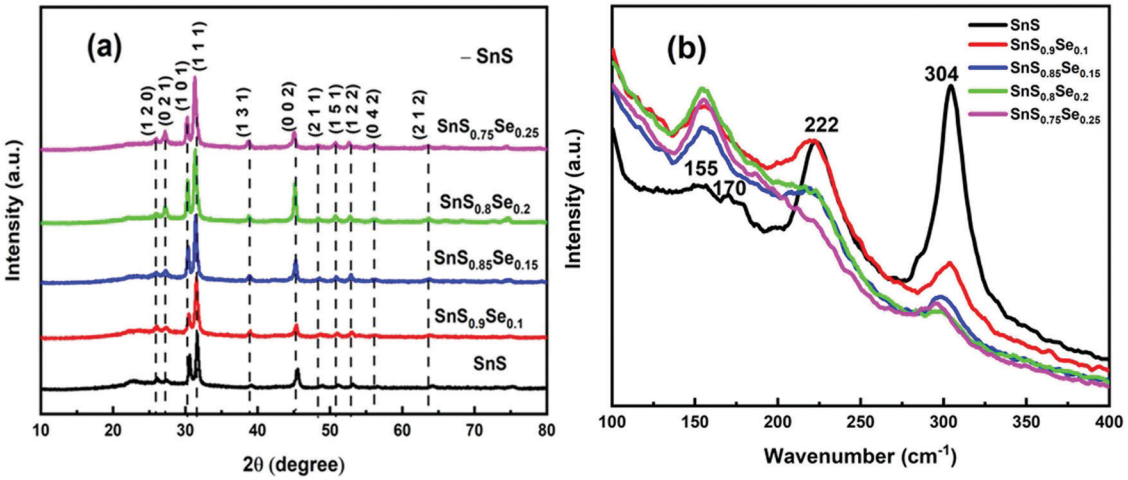

Fig. 1 (a) XRD pattern presenting different phases and (b) Raman spectra of $SnS_{1-x}Se_x$ (x = 0, 0.1, 0.15, 0.2, 0.25) thin films.

of Se doping, which satisfies Vegard's law.[1] According to Vegard's law, the dopant alone cannot produce individual peaks, except the host peak, but it can generate acceptable shifts in the position of the host peak. All the calculated microstructural parameters are tabulated in Table 1.

Scherrer's equation[33] is used to calculate the average crystallite size (D):

$$\text{Crystallite size } (D) = \frac{k\lambda}{\beta \cos\theta} \quad (1)$$

where the Scherrer constant k = 0.94, the Cu Kα line λ = 0.154 nm, β is the full-width at half-maximum in radians, and 'θ' is the Bragg angle. Furthermore, the incorporation of Se affects the microstructural parameters like lattice strain (ε), dislocation density (δ), and the number of crystallites per unit surface area (N). The microstructural parameters were calculated using the following relations:[34]

$$\delta = \frac{1}{D^2}, \quad \varepsilon = \frac{\beta}{4\tan\theta}, \quad N = \frac{t}{D^3}, \quad (2)$$

where 't' is the film thickness. The evaluated quantities are presented in Table 1, which shows that the average crystallite size increased with the increase of Se doping in the SnS film up to 0.2 and then decreased with further Se doping as reported by Kafashan *et al.*[35] The increase of crystallinity might have occurred for the formation of new nucleation centers from the dopant atoms. However, further Se doping results in saturation nucleation and leads to a mismatch in the SnS lattice, resulting in decreased crystallinity. There is a decrease in strain and dislocation density with Se doping, which ensures the increase in the crystallinity of the compound. The N value decreases with Se doping.

Table 1 Microstructural parameters of undoped and Se doped $SnS_{1-x}Se_x$ thin films

Sample	Crystallite size (D) in m ($\times 10^{-8}$)	Dislocation density (δ) in m^{-2} ($\times 10^{15}$)	Strain (ε) ($\times 10^{-4}$)	N (1 m^{-2}) ($\times 10^{17}$)
SnS	1.668	3.591	64.5	1.721
$SnS_{0.9}Se_{0.1}$	1.679	3.546	68	1.689
$SnS_{0.85}Se_{0.15}$	1.691	3.493	67.1	1.659
$SnS_{0.8}Se_{0.2}$	1.876	2.840	58.4	1.211
$SnS_{0.75}Se_{0.25}$	1.737	1.737	66	1.524

3.2. Raman analysis

Raman spectroscopy is an important characterization technique which helps to analyze information regarding molecular interactions, chemical structures, and crystal phases. The vibrational band analysis gives important information about phase transitions and structural rearrangements due to Se doping. The Raman data of the $SnS_{1-x}Se_x$ film in the range of 100–400 cm^{-1} are shown in Fig. 1(b). The Raman bands of the as-prepared tin sulphide thin film are centered at 155, 170, 222, and 304 cm^{-1}, respectively. Li *et al.* have reported the presence of a Raman band at 150 cm^{-1} for the A_g mode of SnSe, which shows that the observed band at 155 cm^{-1} can be attributed to the A_g phase of SnSe.[18] The intensity of the SnSe band with the A_g mode increased with the concentration of Se doping. The 170 cm^{-1} vibrational band is due to the B_{3g} mode of SnS.[36] The B_{3g} mode that appeared at 170 cm^{-1} disappeared for all other Se doped samples. Tian *et al.* reported the A_g mode of the SnS band that appeared at a peak position of 218.7 (cm^{-1}).[17] Thus, the 222 cm^{-1} band is assigned to the A_g mode of SnS, whose intensity decreased with the incorporation of Se. From the Raman spectra, the most intense peak at 304 cm^{-1} is probably due to the Sn_2S_3 phase, as reported earlier by Reddy *et al.*, in which the band intensity decreased with Se doping.[37] Thus, from the Raman spectra, it is observed that the vibrational bands become broader and show a redshift with an increase of Se doping concentration compared to the undoped SnS sample. Thus, the formation of different bands and changes in their intensity and position led to structural changes due to the variation of Se in $SnS_{1-x}Se_x$ samples.

3.3. FESEM and EDX studies

The 1 μm FESEM images of the $SnS_{1-x}Se_x$ films with different Se concentrations are shown in Fig. 2. Remarkable changes in

the surface morphology of $SnS_{1-x}Se_x$ films are observed due to the incorporation of Se in the SnS film. From the figure, it can be observed that the tin sulphide sample shows a densely packed nanoflake-like morphological structure. The columnar grain growth of SnS might have been caused by the 2D growth nature of SnS.[38] It can be clearly seen that the grain size increased with the increase in the Se concentration. The improvements in the uniformity and packing of grains are due to the Se incorporation which results in an enhancement in reflectance properties.[35] But a higher doping concentration of Se can lead to a decrease in the grain size again. These morphological variations may be due to Se incorporation. From the XRD data, the intensity of the peak at (1 1 1) increased with Se incorporation, but for a higher amount of Se incorporation (x = 0.25), the peak intensity decreased. A similar trend was observed for the FESEM grain size. Thus, there is a good correlation between XRD and FESEM data.

The EDX images show the presence of all the elements (Sn, S, Se) in the investigated $SnS_{1-x}Se_x$ films without any contamination. The EDX and FESEM images are shown in Fig. 2, which represent the different peaks corresponding to their respective elements. Furthermore, the related atomic percentage of the elements was calculated from the peak intensities and the area under the peak of the corresponding elements. A systematic increase in the atomic percentage of the Se content is found from the EDX analysis, which is in accordance with the increase of the Se dopant in the SnS film.

3.4. Optical properties

3.4.1. Transmission (T), absorption coefficient (α), extinction coefficient (k), bandgap (E_g), and Urbach energy (E_u). Transmission (T) is a basic optical parameter that indicates the % of transmitted light through an optical medium. Materials with a high transmission are used in many potential applications like optoelectronic sensors and photonic devices. Fig. 3(a) shows the transmittance spectra of ternary $SnS_{1-x}Se_x$ films in the wavelength range of 900–1100 nm. The transmission percentage decreased with Se doping. The films become more absorbing for which there is a decrease in the transmittance with an increase in Se doping. The decrease in transmittance is also due to the crystallization of the film structure by increasing the crystallite size with Se doping as observed from the XRD study. The absorption edge of the film showed a redshift with the Se content. The addition of 'Se' atoms increases the interconnection between the film atoms as they form more heteropolar bonds in the film. In addition, the Se element has a lower bandgap than S. Thus, incorporation of Se in the SnS film enhances the absorption of the samples and leads to a redshift of the absorption edge. Similar results have also been reported by Banotra *et al.*[32] According to their explanation, the decrease in the transmittance percentage is ascribed to the grain boundaries and lattice defects that exist in the film due to the interaction of Se ions.

The absorption coefficient (α) gives the ability to absorb electromagnetic radiation when it passes through a material. The information regarding the band structure and optical bandgap of the film can be extracted by using the absorption coefficient data. The 'α' value is calculated by using the formula:[39]

$$\alpha = \frac{1}{t}\ln\frac{(1-R)^2}{T} \quad (3)$$

where 't' is the film thickness (~800 nm), 'T' represents the transmittance and 'R' represents the reflectance of the films. The absorption coefficient graph of the $SnS_{1-x}Se_x$ films is shown in Fig. 3(b), which reveals the α value in the order of 10^4–10^5 cm^{-1} and is reduced with wavelength. The decrease of 'α' with wavelength indicated an increase in the transparency of the film at a higher wavelength and became suitable for light waves to propagate faster and easier. Moreover, the α value increased with the

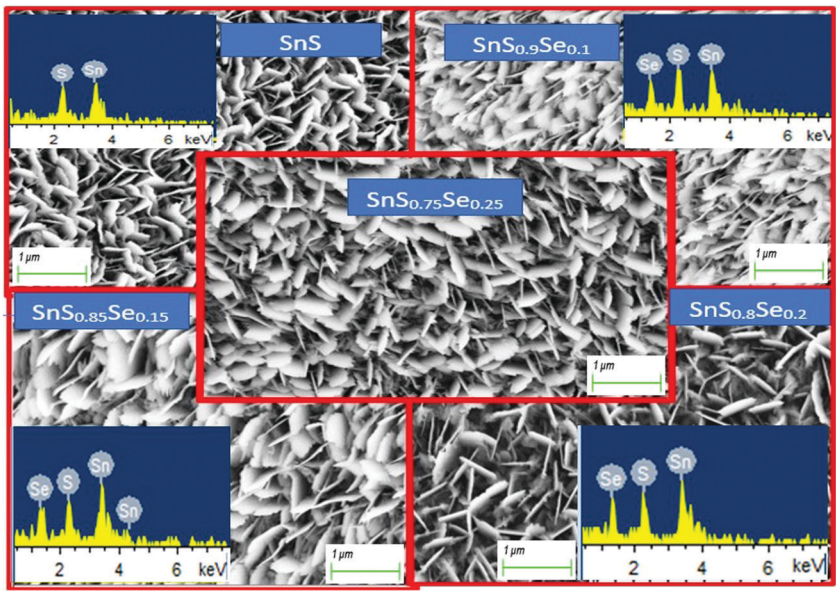

Fig. 2 FESEM images of $SnS_{1-x}Se_x$ (x = 0, 0.1, 0.15, 0.2, 0.25) thin films and their corresponding EDX images (inset).

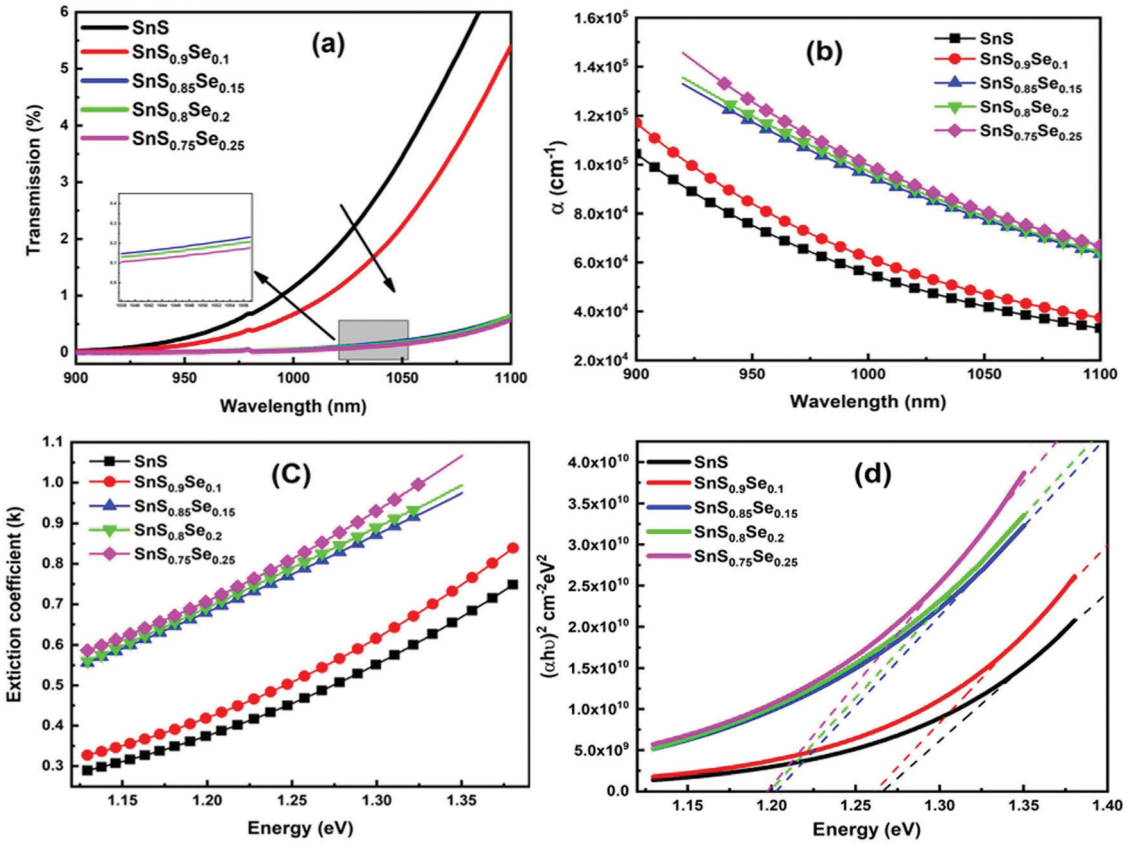

Fig. 3 (a) Transmittance spectra of $SnS_{1-x}Se_x$ (x = 0, 0.1, 0.15, 0.2, 0.25) thin films, (b) change in the absorption coefficient (α) with Se concentration, (c) variation of the extinction coefficient (k), and (d) estimation of the direct bandgap for different Se concentration films.

increase of the Se doping concentration and reached the order of 10^5 cm^{-1} which is more than 2–3 $\times$ 10^4 cm^{-1} as reported.[40] Therefore, the sample can be used as an excellent solar absorber in the field of photovoltaics with a significantly lower thickness.

The extinction coefficient (k) is calculated in terms of 'α' and 'λ' by using the relation:[41]

$$k = \frac{\alpha\lambda}{4\pi} \quad (4)$$

The surface smoothness and homogeneity of the sample were analyzed from the extinction coefficient (k) data. Fig. 3(c) shows the variation of the extinction coefficient with photon energy. It is noticed that the extinction coefficient increased with the incident energy as well as with the Se doping concentration. The increase in 'k' with energy and its decrease with wavelength represent the light dispersion and drop in absorption, respectively. The low 'k' value for the pure SnS sample indicates a smooth and homogeneous surface of the films. But, with an increase in Se doping, the 'k' value increased, which shows a decrease in surface smoothness as confirmed by the structural analysis.

The optical bandgap energy (E_g) plays an essential role in selecting the semiconducting materials for potential applications. According to Tauc, the energy required to transport an electron through a forbidden bandgap depends on the intrinsic behavior of the film and the photon energy in semiconducting materials.[42] For a semiconducting material, the absorption strength of the incident electromagnetic waves depends on the difference between bandgap energy (E_g) and incident photon energy ($h\nu$). Here, Tauc's formula is used to calculate the energy gap in the high absorption region ($\alpha \geq 10^4$ cm^{-1}) by using[43]

$$\alpha h\nu = B(h\nu - E_g)^m \quad (5)$$

where 'ν' represents the incident frequency, 'B' is the band tail parameter which depends upon the transition probability, and 'm' is the transition mode power factor which depends on the type of electronic transition. For different transitions, 'm' has different values, *i.e.*, m = 1/2 for direct allowed transitions, 2 for indirect allowed transitions, 3/2 for direct forbidden transitions, and 3 for indirect forbidden transitions. As per the Tauc rule, indirect transitions are observed for amorphous materials and direct allowed transitions for crystalline materials. Since both undoped and selenium doped films show a crystalline nature, m = 1/2 was substituted in eqn (5) to evaluate the direct allowed energy gap, and the plot between $(\alpha h\nu)^2$ *vs.* $h\upsilon$ is shown in Fig. 3(d). The E_g value is taken from the intercept of the graph, and the slope gives the Tauc parameter (B). The obtained values of both 'E_g' and 'B' are presented in Table 2. It is found that the bandgap value decreased from 1.265 $\pm$ 0.001 eV to 1.197 $\pm$ 0.001 eV with an increase in Se%. Wang *et al.* also reported similar results, where the optical bandgap decreased

from 1.15 to 1.01 eV with Se doping.[44] The material having a small bandgap can block both visible light and infrared light transmission. Moreover, these materials possess a unique ability to filter the ultraviolet part from electromagnetic radiation. This property makes thin films of smaller bandgaps suitable for solar applications and thermal systems.[45] The slope of the graph gives the '*B*' value, which is inversely proportional to the degree of disorder. It is observed from Table 2 that '*B*' increases with selenium doping.

According to Urbach, near the absorption edge of semiconducting materials, there is an exponential region that describes the width of the band tail of the material. This band tail represents the localized states.[46] The absorption coefficient for most of the semiconducting material depends on '$h\nu$' near the band edge, satisfying the Urbach empirical formula:[47]

$$\alpha(h\nu) = \alpha_0 \exp\left(\frac{h\nu}{E_u}\right) \quad (6)$$

where 'α_0' is the constant value corresponding to the absorption coefficient at the band gap energy and 'E_u' is the Urbach energy. The E_u parameter measures the degree of disorder in the material, which is the inverse of the slope obtained from the graph between $h\upsilon$ and $\ln(\alpha/\alpha_0)$. The obtained E_u values are tabulated in Table 2, which shows an increasing trend, while the optical bandgap decreases with selenium doping. This might be due to the incorporation of selenium, which increases the localized states within the bandgap region. Davis and Mott's[48] model infers that the localized states within the band structure are the reason for the reduction of the bandgap. Thus, our results seem to have a good agreement with Davis and Mott's discussion.

3.4.2. Optical density and skin depth. Optical density (OD) is associated with the absorption of light, which indicates the absorbing power of a material towards electromagnetic radiation. The optical density is proportional to both the thickness and concentration of the absorbing material. The optical density of $SnS_{1-x}Se_x$ is calculated by using the simple formula:[49] $OD = \alpha \times t$, where '*t*' is the film thickness. Fig. 4(a) shows the change in OD with wavelength. It is observed that the variation of OD, with either wavelength or incident energy, shows a similar behaviour to the absorption coefficient where the thickness of all the samples is constant.[50] In the intense absorption spectral regions, all the energy that enters the thin film is either absorbed or reflected. Here, skin depth is one of the important parameters which is related to the absorption of photons within the thin film texture. The photon density decreased in an exponential way from the surface towards the midway of the film. This happens due to many factors like the film density, surface morphology, refractive index, and microstructure of the films. Skin depth (δ) is defined as the thickness at which the density of photons becomes $1/e$ of the value at the surface. The conductivity of the film and the incident photon energy also affect the value of skin depth. As the conductivity of the semiconductor material and optical bandgap are strongly dependent, one can relate the optical quantities and skin depth (penetration depth) in any semiconducting material.[51] The skin depth is calculated by using the α value by[52] $\delta = \frac{1}{\alpha}$. The variation of '$\delta$' with '$h\nu$' is shown in Fig. 4(b). It is observed that 'δ' decreased with the increase of '$h\nu$' as well as with the Se content. The increase in the Se content leads to a decrease in the transparency of the film.

3.4.3. Static refractive index, dielectric constant (ε_∞), and optical electronegativity (η_{Opt}). The linear static refractive index (n_0) and high-frequency dielectric constant (ε_∞) of the sample are related by the equation: $\varepsilon_\infty = {n_0}^2$. The n_0 value is calculated by using the Dimitrov and Sakka relation:[53]

$$\frac{{n_0}^2 - 1}{{n_0}^2 + 2} = 1 - \sqrt{\frac{E_g}{20}} \quad (7)$$

where 'E_g' is the bandgap. The calculated values of n_0 and ε_∞ are presented in Table 2. The calculated data clearly show the increase in the refractive index with the increase of selenium concentration in $SnS_{1-x}Se_x$ films. Generally, the obtained results are in good agreement with the literature.[54] The increase in the refractive index can be attributed to an increase in density by substituting sulphur with a larger amount of selenium.[55] From Table 2, it can be observed that the dielectric constant of the lattice increased with the increase in selenium doping. Furthermore, optical electronegativity has a crucial role in determining various physicochemical constants of the material. The parameter η_{opt} is defined as the ability of atoms or radicals to form ionic bonds due to their tendency to attract electrons. According to Duffy, the optical electronegativity (η_{opt}) values are determined using the value of n_0 as follows:[56] $\eta_{opt} = \left(\frac{C}{n_0}\right)^{\frac{1}{4}}$, where C is the dimensionless quantity having a value of 25.54. The optical electronegativity values are presented in Table 2. It is

Table 2 Optical parameters of $SnS_{1-x}Se_x$ thin films

Estimated optical parameters	SnS	$SnS_{0.9}Se_{0.1}$	$SnS_{0.85}Se_{0.15}$	$SnS_{0.8}Se_{0.2}$	$SnS_{0.75}Se_{0.25}$
Optical band gap (direct E_g) in eV	1.265 ± 0.001	1.261 ± 0.002	1.202 ± 0.001	1.198 ± 0.001	1.197 ± 0.001
Tauc parameter (B^2) in cm^{-2} eV^{-2}	1.797×10^{11}	2.161×10^{11}	2.184×10^{11}	2.213×10^{11}	2.465×10^{11}
Urbach energy (E_u) in eV	0.218	0.219	0.295	0.303	0.282
Static refractive index (n_0)	3.150	3.154	3.199	3.202	3.203
Dielectric constant of the lattice (ε_∞)	9.924	9.945	10.235	10.254	10.261
First-order nonlinear susceptibility (χ^1)	0.710	0.712	0.735	0.736	0.737
Third-order nonlinear susceptibility (χ^3)	4.333×10^{-11}	4.374×10^{-11}	4.968×10^{-11}	5.009×10^{-11}	5.024×10^{-11}
Nonlinear refractive index (n_2)	5.182×10^{-10}	5.226×10^{-10}	5.851×10^{-10}	5.895×10^{-10}	5.910×10^{-10}
Optical electronegativity (η_{opt})	1.6874	1.6869	1.6809	1.6805	1.6803

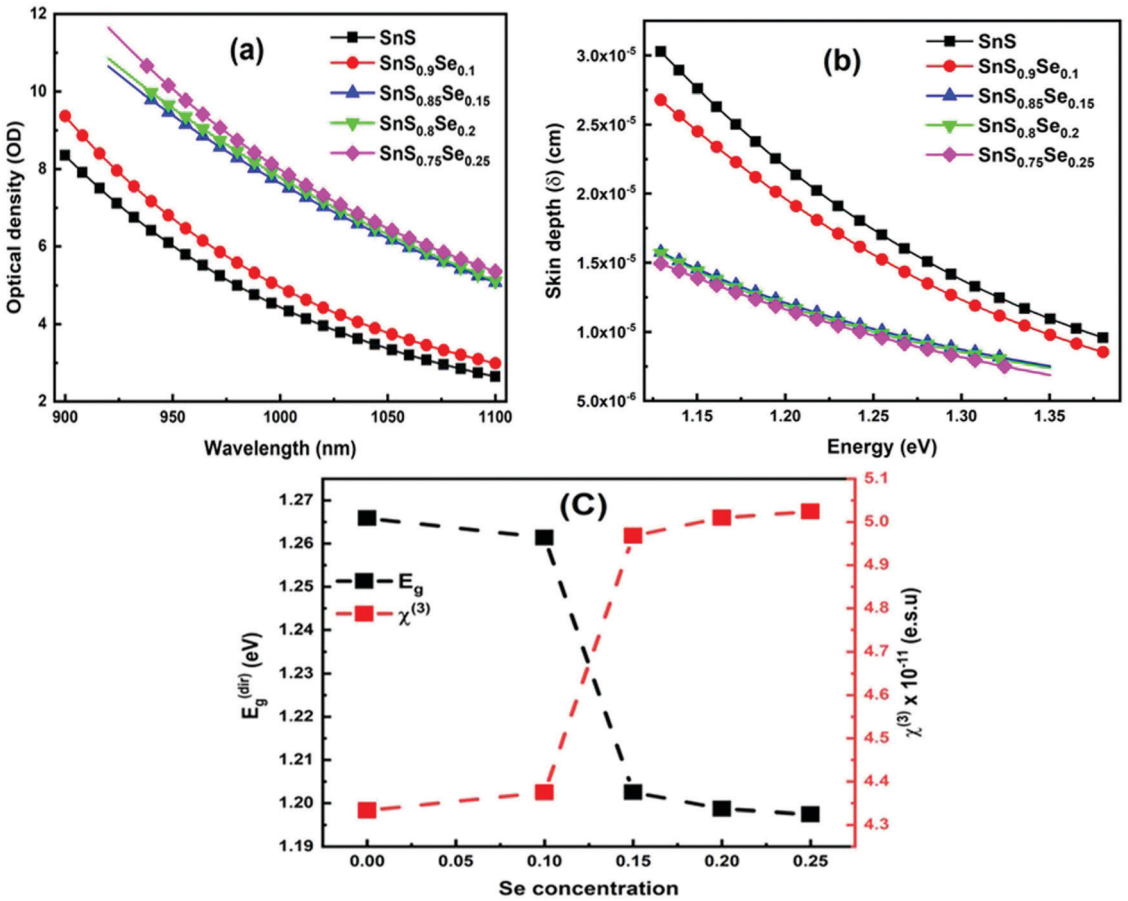

Fig. 4 (a) Change in the optical density of $SnS_{1-x}Se_x$ (x = 0, 0.1, 0.15, 0.2, 0.25) thin films, (b) skin depth of $SnS_{1-x}Se_x$ with energy, and (c) variation of E_g and χ^3 with Se doping concentration.

observed that the value of η_{opt} decreased from 1.6874 to 1.6803 as the Se content increased in the $SnS_{1-x}Se_x$ thin film.[57]

3.4.4. Nonlinear optical parameters. The nonlinear optical response of a material is demonstrated by sufficient intense illumination and also depends on the strength of the electric field, which causes nonlinear effects in the films. The nonlinear behaviour originates from the interaction of the nucleus due to electronic polarizability and its effect on the bond length. The polarization density $P(t)$ is presented by a power series expansion of the total applied optical field:[58]

$$P(t) = \varepsilon_0[\chi^{(1)}E(t) + \chi^{(2)}E^{(2)}(t) + \chi^{(3)}E^{(3)}(t)] \quad (8)$$

where 'E' refers to the electric field intensity and $\chi^{(1)}$ represents the linear behaviour, whereas $\chi^{(2)}$ and $\chi^{(3)}$ represent the second- and third-order nonlinear susceptibility, respectively. The value of $\chi^{(2)}$ is zero for centrosymmetric optically isolated materials.[59] Therefore, $\chi^{(3)}$ is a superior nonlinear quantity. So the nonlinear susceptibilities $\chi^{(1)}$ and $\chi^{(3)}$ of the semiconducting material are calculated using Miller's rule as follows:[60]

$$\chi^{(1)} = \frac{(n_0^2 - 1)}{4\pi}, \quad \chi^{(3)} \cong A\left(\chi^{(1)}\right)^4, \quad (9)$$

where $A = 1.7 \times 10^{-10}$ (e.s.u.) and n_0 refers to the static refractive index at $h\nu \rightarrow 0$. The calculated $\chi^{(1)}$ and $\chi^{(3)}$ values are presented in Table 2. It is observed that both $\chi^{(1)}$ and $\chi^{(3)}$ increased with the Se content due to the increase in the n_0 value. The increased nonlinear susceptibility makes the material suitable for use in small, compact, and low-power devices for telecommunication purposes.[61] The change in E_g and $\chi^{(3)}$ with the Se content is shown in Fig. 4(c) which infers an opposite change for the parameters with the Se percentage in ternary $SnS_{1-x}Se_x$ films. Furthermore, the static refractive index is used to calculate the nonlinear refractive index (n_2) by applying the Ticha and Tichy relation with Miller's generalized rule as follows:[62] $n_2 = \frac{12\pi\chi^{(3)}}{n_0}$. The calculated values of 'n_2' are shown in Table 2, which indicates that the value of n_2 increased with the Se%, which is for the increase of the refractive index with selenium addition. The high value of the nonlinear refractive index makes the $SnS_{1-x}Se_x$ films suitable candidates for nonlinear optical applications.

3.5. Theoretical calculations of different physical parameters

3.5.1. Number of constraints and the effective coordination number. Loffe and Regel demonstrated the bonding characteristics in the nearest neighbor region which shows that the coordination number represents the electronic properties of

Table 3 Physical parameters of $SnS_{1-x}Se_x$ (x = 0, 0.1, 0.15, 0.2, 0.25) thin films

Sample	N_{avg}	N_α	N_β	$N = (N_\alpha + N_\beta)$	$\overline{H_s}$	V_{av}	L
SnS	3	1.5	3	4.5	64.5	5	2
$SnS_{0.9}Se_{0.1}$	3	1.5	3	4.5	64.12	5	2
$SnS_{0.85}Se_{0.15}$	3	1.5	3	4.5	63.93	5	2
$SnS_{0.8}Se_{0.2}$	3	1.5	3	4.5	63.74	5	2
$SnS_{0.75}Se_{0.25}$	3	1.5	3	4.5	63.55	5	2

semiconducting materials.[63] The average coordination number (N_{avg}) is calculated by

$$N_{avg} = \frac{xN_{Sn} + yN_S + zN_{Se}}{x + y + z} \quad (10)$$

where x, y, and z indicate the atomic % of Sn, S, and Se, respectively, and N_{Sn}, N_S, and N_{Se} represent the coordination numbers of Sn, S, and Se, having values of 4, 2, and 2, respectively. The corresponding N_{avg} values of the samples are calculated and presented in Table 3.

According to Phillips and Thorpe's topological constraint theory, the rigidity of amorphous materials can be calculated by computing the number of constraints experienced by each atom.[64] The constraints such as two-body radial band stretching (N_α) and three-body angular constraints (N_β) are involved in a covalent-like network. These constraint values are calculated by using the average coordination number through the following formula:

$$N_\alpha = \frac{N_{avg}}{2} \text{ and } N_\beta = 2N_{avg} - 3 \quad (11)$$

Total mechanical constraints per atom were calculated by adding the above two values ($N = N_\alpha + N_\beta$) and are presented in Table 3.

3.5.2. The average heat of atomization ($\overline{H_s}$) and lone pair of electrons (L). The optical bandgap is correlated with the chemical bond energy which is related to the average heat of atomization (H_s). H_s is defined as the quantity of heat energy required to change 1 mol of an element in its standard state at 298 K to the gaseous state. For the compound $A_xB_yC_z$, the average heat of atomization is calculated by[65]

$$\overline{H_s} = \frac{xH_{Sn} + yH_S + zH_{Se}}{x + y + z} \quad (12)$$

where x, y, and z are the atomic % of Sn, S, and Se, respectively. H_{Sn}, H_S, and H_{Se} represent the H_s values of Sn, S, and Se (72, 57, and 49.4 kcal g^{-1} atom), respectively. The average heat of atomization of the samples is calculated and presented in Table 3. From the table, it is observed that the H_s value decreased with the increase of the Se percentage.[66] Lone pair electrons are defined as nonbonded electrons present in the valence shell. Although lone pair electrons are nonbonded, these can deform a bond more easily than a bond with no shared electrons. The number of lone pair electrons is calculated through the relation:[67] $L = V_{avg} - N_{avg}$, where N_{avg} is the average coordination number and V_{avg} is the average valence electrons and expressed as $V_{avg} = \frac{xV_{Sn} + yV_S + zV_{Se}}{(x + y + z)}$, where V_{Sn}, V_S, and V_{Se} are the valence of Sn, S, and Se which are equal to 4, 6, and 6, respectively. The calculated lone pair electrons are listed in Table 3. The cohesive energy of the present system is calculated using heteronuclear and homonuclear bonds based on the chemical bond approach. The heteronuclear bond energy is calculated from the relation:[45]

$$C(A–B) = [C(A–A) \times C(B–B)]^{1/2} + 30(\chi^A - \chi^B)^2 \quad (13)$$

where χ^A and χ^B are the electro-negativity values of the constituent elements Sn, S, and Se, having the values of 1.88, 2.58, and 2.55, respectively. The homonuclear bond energies of Sn–Sn, S–S, and Se–Se are 44.71, 53.8, and 44.04 kcal mol^{-1}, respectively.[68] The heteronuclear bond energies of Sn–S, Sn–Se, and S–Se, calculated using the above equation are 63.74, 57.83, and 48.70 kcal mol^{-1}, respectively. The Sn–S bond is expected to form first, as the bond energy of the Sn–S heteropolar bond is more than that of the other bond involved in the present system. After that, Sn–Se and S–S bonds are formed according to the calculated bond energies. Se is doped into the SnS host matrix in the present $SnS_{1-x}Se_x$ system. Thus, Se atoms prefer to form Sn–Se and S–Se heteropolar bonds. After heteropolar bond formation, there are still unsatisfied Sn and S valences to form homopolar bonds. Thus, there are more homopolar bonds than heteropolar bonds, which leads to more disorder in the system. Due to the presence of group VI elements, there are a large number of lone pair electrons which form the top of the valence band, whereas the antibonding electrons form the bottom of the conduction band. Due to the presence of high-energy lone pair electrons, metal atoms can form dative bonds with group VI elements.[68] The localized acceptor states in the gap increased due to the antibonding levels corresponding to the dative bond. Thus, the increased localized state in the gap reduces the optical bandgap.[69]

4. Conclusion

Ternary $SnS_{1-x}Se_x$ films were prepared by the thermal evaporation technique at different Se concentrations. This study is focused on changes in their structural and linear/nonlinear optical properties due to Se doping. The XRD spectra of the prepared $SnS_{1-x}Se_x$ thin films show the crystallinity nature of the pure SnS phase. The crystallinity increased with the increase of Se content due to the formation of new nucleation centers from the dopant atoms. The variation of Se% greatly affects the surface morphology of the film. An increase in the size and density of nanoflake-like structures can be noticed from the FESEM images. The systematic increase in the Se concentration due to doping is confirmed by the EDX analysis. The transmission percentage of the $SnS_{1-x}Se_x$ films decreased with Se doping, whereas the absorption coefficient and extinction coefficient values increased with Se%. The direct optical bandgap reduced from 1.265 ± 0.001 to 1.197 ± 0.001 eV with Se%. The optical density decreased, whereas the skin depth increased with the Se content. The static refractive index (n_0) increased with Se%, further helping to increase the

nonlinearity of the films. The nonlinearity parameters like first-order and third-order susceptibility ($\chi^{(3)}$) and the nonlinear refractive index increased with the doping concentration. The average heat of atomization decreased with Se content. These properties make the studied thin films with smaller bandgaps suitable for solar and thermal applications.

Conflicts of interest

There are no conflicts of interest regarding this manuscript.

Acknowledgements

R. Naik thanks the Department of Physics, IISc, Bangalore, for optical, FESEM, and Raman measurements. Dr Naik also thanks ICT-IOCB for the Start-up Research grant.

References

1 M. D. Khan, M. Aamir, G. Murtaza, M. A. Malik and N. Revaprasadu, Structural investigations of $SnS_{1-x}Se_x$ solid solution synthesized from chalcogeno-carboxylate complexes of organo-tin by colloidal and solvent-less routes, *Dalton Trans.*, 2018, **47**(30), 10025–10034.

2 R. Fei, W. Li, J. Li and L. Yang, Giant piezoelectricity of monolayer group IV monochalcogenides: SnSe, SnS, GeSe, and GeS, *Appl. Phys. Lett.*, 2015, **107**(17), 173104.

3 C. J. Liu, S. Y. Tai, S. W. Chou, Y. C. Yu, K. D. Chang, S. Wang, F. S. S. Chien, J. Y. Lin and T. W. Lin, Facile synthesis of MoS_2/graphene nanocomposite with high catalytic activity toward triiodide reduction in dye-sensitized solar cells, *J. Mater. Chem.*, 2012, **22**(39), 21057–21064.

4 H. Liu, A. T. Neal, Z. Zhu, Z. Luo, X. Xu, D. Tománek and P. D. Ye, Phosphorene: An unexplored 2D semiconductor with a high hole mobility, *ACS Nano*, 2014, **8**(4), 4033–4041.

5 A. Gupta, T. Sakthivel and S. Seal, Recent development in 2D materials beyond graphene, *Prog. Mater. Sci.*, 2015, **73**, 44–126.

6 A. S. Pawbake, S. R. Jadkar and D. J. Late, High-performance humidity sensor and photodetector based on SnSe nanorods, *Mater. Res. Express*, 2016, **3**(10), 105038.

7 W. Shi, M. Gao, J. Wei, J. Gao, C. Fan, E. Ashalley, H. Li, Z. Wang, W. R. Shi, M. X. Gao, J. P. Wei, J. F. Gao, C. W. Fan, E. Ashalley, Z. M. Wang and D. Li, Tin Selenide (SnSe): Growth, properties, and applications, *Adv. Sci.*, 2018, **5**(4), 1700602.

8 P. Mandal, B. Show, S. T. Ahmed, D. Banerjee and A. Mondal, Visible-Light Active Electrochemically deposited tin selenide thin films: Synthesis, characterization and photocatalytic activity, *J. Mater. Sci.: Mater. Electron.*, 2020, **31**(6), 4708–4718.

9 Y. Wang, L. Huang, B. Li, J. Shang, C. Xia, C. Fan, H. X. Deng, Z. Wei and J. Li, Composition-tunable 2D $SnSe_{2(1-x)}S_{2x}$ alloys towards efficient bandgap engineering and high performance (Opto)electronics, *J. Mater. Chem. C*, 2016, **5**(1), 84–90.

10 B. Wang, S. P. Zhong, Z. B. Zhang, Z. Q. Zheng, Y. P. Zhang and H. Zhang, Broadband photodetectors based on 2D Group IVA metal chalcogenides semiconductors, *Appl. Mater. Today*, 2019, **15**, 115–138.

11 A. Le Donne, V. Trifiletti and S. Binetti, New earth-abundant thin film solar cells based on chalcogenides, *Front. Chem.*, 2019, 7.

12 R. Guo, X. Wang, Y. Kuang and B. Huang, First-principles study of anisotropic thermoelectric transport properties of IV–VI semiconductor compounds SnSe and SnS, *Phys. Rev. B: Condens. Matter Mater. Phys.*, 2015, **92**(11), 115202.

13 C. Lu, Y. Zhang, L. Zhang and Q. Yin, Preparation and photoelectrochemical properties of SnS/SnSe and SnSe/SnS bilayer structures fabricated *via* electrodeposition, *Appl. Surf. Sci.*, 2019, **484**, 560–567.

14 N. K. Reddy, K. Ramesh, R. Ganesan, K. T. R. Reddy, K. R. Gunasekhar and E. S. R. Gopal, Synthesis and characterisation of co-evaporated tin sulphide thin films, *Appl. Phys. A: Mater. Sci. Process.*, 2006, **83**(1), 133–138.

15 L. A. Burton, D. Colombara, R. D. Abellon, F. C. Grozema, L. M. Peter, T. J. Savenije, G. Dennler and A. Walsh, Synthesis, characterization, and electronic structure of single-crystal SnS, Sn_2S_3, and SnS_2, *Chem. Mater.*, 2013, **25**(24), 4908–4916.

16 B. Ghosh, M. Das, P. Banerjee and S. Das, Fabrication and optical properties of SnS thin films by silar method, *Appl. Surf. Sci.*, 2008, **254**(20), 6436–6440.

17 Z. Tian, C. Guo, M. Zhao, R. Li and J. Xue, Two-dimensional SnS: A phosphorene analogue with strong in-plane electronic anisotropy, *ACS Nano*, 2017, **11**(2), 2219–2226.

18 X. Z. Li, J. Xia, L. Wang, Y. Y. Gu, H. Q. Cheng and X. M. Meng, Layered SnSe nano-plates with excellent in-plane anisotropic properties of Raman spectrum and photoresponse, *Nanoscale*, 2017, **9**(38), 14558–14564.

19 H. Tian, C. Fan, G. Liu, S. Yuan, Y. Zhang, M. Wang and E. Li, Ultrafast broadband photodetector based on SnS synthesized by hydrothermal method, *Appl. Surf. Sci.*, 2019, **487**, 1043–1048.

20 J. Yao, G. Yang, J. Yao and G. Yang, Flexible and high-performance all-2D photodetector for wearable devices, *Small*, 2018, **14**(21), 1704524.

21 J. Xia, D. Zhu, X. Li, L. Wang, L. Tian, J. Li, J. Wang, X. Huang and X. M. Meng, Epitaxy of layered orthorhombic $SnS–SnS_xSe_{(1-x)}$ core–shell heterostructures with anisotropic photoresponse, *Adv. Funct. Mater.*, 2016, **26**(26), 4673–4679.

22 A. Akkari, M. Reghima, C. Guasch and N. Kamoun-Turki, Effect of copper doping on physical properties of nanocrystallized SnS zinc blende thin films grown by chemical bath deposition, *J. Mater. Sci.*, 2012, **47**(3), 1365–1371.

23 K. S. Kumar, A. G. Manohari, S. Dhanapandian and T. Mahalingam, Physical properties of spray pyrolyzed Ag-doped sns thin films for opto-electronic applications, *Mater. Lett.*, 2014, **131**, 167–170.

24 H. Kafashan and Z. Balak, Preparation and characterization of electrodeposited SnS:In thin films: Effect of in dopant, *Spectrochim. Acta, Part A*, 2017, **184**, 151–162.
25 W. Gao, Z. Zheng, L. Huang, J. Yao, Y. Zhao, Y. Xiao and J. Li, Self-powered $SnS_{1-x}Se_x$ alloy/silicon heterojunction photodetectors with high sensitivity in a wide spectral range, *ACS Appl. Mater. Interfaces*, 2019, **11**(43), 40222–40231.
26 K. Santhosh Kumar, C. Manoharan, S. Dhanapandian and A. Gowri Manohari, Effect of Sb dopant on the structural, optical and electrical properties of SnS thin films by spray pyrolysis technique, *Spectrochim. Acta, Part A*, 2013, **115**, 840–844.
27 G. Gordillo, M. Botero and J. S. Oyola, Synthesis and Study of Optical and structural properties of thin films based on new photovoltaic materials, *Microelectron. J.*, 2008, **39**(11), 1351–1353.
28 J. Yu, C. Y. Xu, Y. Li, F. Zhou, X. S. Chen, P. A. Hu and L. Zhen, Ternary $SnS_{2-x}Se_x$ alloys nanosheets and nanosheet assemblies with tunable chemical compositions and band gaps for photodetector applications, *Sci. Rep.*, 2015, **5**(1), 1–10.
29 W. Gao, Y. Li, J. Guo, M. Ni, M. Liao, H. Mo and J. Li, Narrow-gap physical vapour deposition synthesis of ultrathin $SnS_{1-x}Se_x$ ($0 \leq x \leq 1$) two-dimensional alloys with unique polarized Raman spectra and high (opto)electronic properties, *Nanoscale*, 2018, **10**(18), 8787–8795.
30 Y. M. Han, J. Zhao, M. Zhou, X. X. Jiang, H. Q. Leng and L. F. Li, Thermoelectric performance of SnS and SnS–SnSe solid solution, *J. Mater. Chem. A*, 2015, **3**(8), 4555–4559.
31 K. Saritha, S. Rasool, K. T. Ramakrishna Reddy, A. M. Saad, M. S. Tivanov, S. E. Tikoto, O. V. Korolik and V. F. Gremenok, Substrate Temperature dependent physical properties of $SnS_{1-x}Se_x$ thin films, *Appl. Phys. A: Mater. Sci. Process.*, 2019, **125**(10), 1–13.
32 A. Banotra and N. Padha, Facile growth of SnS and $SnS_{0.40}Se_{0.60}$ thin films as an absorber layer in the solar cell structure, *Mater. Today: Proc.*, 2020, **26**, 3420–3425.
33 D. J. Lim, N. A. Marks and M. R. Rowles, Universal Scherrer equation for graphene fragments, *Carbon*, 2020, **162**, 475–480.
34 P. Priyadarshini, S. Das, D. Alagarasan, R. Ganesan, S. Varadharajaperumal and R. Naik, Observation of high nonlinearity in Bi-doped $Bi_xIn_{35-x}Se_{65}$ thin films with annealing, *Sci. Rep.*, 2021, **11**, 21518.
35 H. Kafashan, M. Azizieh and Z. Balak, Electrochemical synthesis of nanostructured Se-doped SnS: Effect of Se-dopant on surface characterizations, *Appl. Surf. Sci.*, 2017, **410**, 186–195.
36 J. Xia, X. Z. Li, X. Huang, N. Mao, D. D. Zhu, L. Wang, H. Xu and X. M. Meng, Physical vapor deposition synthesis of two-dimensional orthorhombic SnS flakes with strong angle/temperature-dependent Raman responses, *Nanoscale*, 2016, **8**(4), 2063–2070.
37 T. S. Reddy and M. C. S. Kumar, Effect of substrate temperature on the physical properties of co-evaporated Sn_2S_3 thin films, *Ceram. Int.*, 2016, **42**(10), 12262–12269.
38 H. Zhu, D. Yang, Y. Ji, H. Zhang and X. Shen, Two-dimensional SnS nanosheets fabricated by a novel hydrothermal method, *J. Mater. Sci.*, 2005, **40**(3), 591–595.
39 P. Pradhan, R. Naik, N. Das and A. K. Panda, Band gap tuning in $As_{40}Se_{53}Sb_{07}$ thin films by 532 nm laser irradiation: An optical investigation by spectroscopic techniques, *Opt. Mater.*, 2018, **75**, 699–709.
40 J. Vidal, S. Lany, M. D'Avezac, A. Zunger, A. Zakutayev, J. Francis and J. Tate, Band-structure, optical properties, and defect physics of the photovoltaic semiconductor SnS, *Appl. Phys. Lett.*, 2012, **100**(3), 032104.
41 R. Naik, A. Aparimita, C. Sripan and R. Ganesan, Structural, linear and non-linear optical properties of annealed and irradiated Ag/Se heterostructure films for optoelectronic applications, *Optik*, 2019, **194**, 162894.
42 J. Tauc, Optical properties and electronic structure of amorphous Ge and Si, *Mater. Res. Bull.*, 1968, **3**(1), 37–46.
43 J. Tauc, Optical properties of amorphous semiconductors, *Amorphous Liq. Semicond.*, 1974, 159–220.
44 S. Wang, X. Lai, B. Du, J. Ma, P. Wang and J. Jian, Synthesis and optical properties of single-crystalline $SnS_{1-x}Se_x$ nanobelts, *Powder Diffr.*, 2020, **35**(4), 276–281.
45 Z. A. Alrowaili, M. M. Soraya, T. A. Alsultani, A. Qasem, E. R. Shaaban and M. Ezzeldien, Sn-induced changes in the structure and optical properties of amorphous As–Se–Sn thin films for optical devices, *Appl. Phys. A: Mater. Sci. Process.*, 2021, **127**(2), 1–11.
46 A. S. Hassanien and A. A. Akl, Effect of Se addition on optical and electrical properties of chalcogenide CdSSe thin films, *Superlattices Microstruct.*, 2016, **89**, 153–169.
47 r Naik, r Ganesan and K. S. Sangunni, Compositional dependence on the optical properties of amorphous $As_{2-x}S_{3-x}Sb_x$ thin films, *Thin Solid Films*, 2010, **518**(19), 5437–5441.
48 A. S. Hassanien and I. Sharma, Optical properties of quaternary A-$Ge_{15-x}Sb_x$ Se_{50} Te_{35} thermally evaporated thin-films: Refractive index dispersion and single oscillator parameters, *Optik*, 2020, **200**, 163415.
49 A. S. Hassanien and A. A. Akl, Influence of composition on optical and dispersion parameters of thermally evaporated non-crystalline $Cd_{50}S_{50-x}Se_x$ thin films, *J. Alloys Compd.*, 2015, **648**, 280–290.
50 I. Sharma, Reddy Madara and S. Sharma, P. Study of Tauc Gap, Optical density and penetration depth of vacuum evaporated $Pb_{15}Se_{85-x}Ge_x$ (X = 0, 3, 6 at%) thin films supported by chemical bond approach and physical parameters, *Mater. Today: Proc.*, 2020, **28**, 402–407.
51 D. Sahoo, P. Priyadarshini, R. Dandela, D. Alagarasan, R. Ganesan, S. Varadharajaperumal and R. Naik, Investigation of amorphous-crystalline transformation induced optical and electronic properties change in annealed $As_{50}Se_{50}$ thin films, *Opt. Quantum Electron.*, 2021, **53**(4), 1–25.
52 N. F. Habubi, S. F. Oboudi and S. S. Chiad, Study of some optical properties of mixed SnO_2–CuO thin films, *J. Nano-Electron. Phys.*, 2012, **4**, 04008.
53 V. Dimitrov and S. Sakka, Linear and nonlinear optical properties of simple oxides. II, *J. Appl. Phys.*, 1998, **79**(3), 1741.
54 P. Sharma, K. A. Aly, D. C. Sati and A. Dahshan, Improvement in the linear and nonlinear optical properties of Mn-

doped $GeSe_2$ chalcogenide thin films for all optical applications, *Appl. Phys. A: Mater. Sci. Process.*, 2020, **126**(3), 1–9.

55 I. Sharma and A. S. Hassanien, Effect of Ge-addition on physical and optical properties of chalcogenide $Pb_{10}Se_{90-x}Ge_x$ bulk glasses and thin films, *J. Non-Cryst. Solids*, 2020, **548**, 120326.

56 R. R. Reddy, K. Rama Gopal, K. Narasimhulu, L. S. S. Reddy, K. R. Kumar, C. V. K. Reddy and S. N. Ahmed, Correlation between optical electronegativity and refractive index of ternary chalcopyrites, semiconductors, insulators, oxides and alkali halides, *Opt. Mater.*, 2008, **31**(2), 209–212.

57 A. S. Hassanien, I. Sharma and K. A. Aly, Linear and non-linear optical studies of thermally evaporated chalcogenide a-Pb–Se–Ge thin films, *Phys. B*, 2021, **613**, 412985.

58 E. Sharma, P. B. Barman and P. Sharma, Evaluation of Optical Linear and Non-Linear Parameters of Thermally deposited GeTeSeGa thin films in nir (1–2.6 μm) wavelength range from their transmission spectra, *Optik*, 2020, **219**, 165181.

59 K. Tanaka, *Optical nonlinearity in photonic glasses*, Springer Handbooks, 2017, p.1.

60 A. S. Hassanien, H. R. Alamri and I. M. El Radaf, Impact of film thickness on optical properties and optoelectrical parameters of novel $CuGaGeSe_4$ thin films synthesized by electron beam deposition, *Opt. Quantum Electron.*, 2020, **52**(7), 1–18.

61 E. R. Shaaban, M. Mohamed, M. N. Abd-el Salam, A. Y. Abdel-Latief, M. A. Abdel-Rahim and E. S. Yousef, Structural, linear and non-linear optical properties of annealed $As_{47.5}Se_{47.5}Ag_5$ thin films for optoelectronic applications, *Opt. Mater.*, 2018, **86**, 318–325.

62 I. Sharma, S. K. Tripathi and P. B. Barman, Effect of deposition parameters and semi-empirical relations between non-linear refractive index with linear refractive index and third order susceptibility for a-$Ge_{20}Se_{70-x}In_{10}Bi_x$ thin films, *J. Appl. Phys.*, 2011, **110**(4), 043108.

63 A. A. Othman, K. A. Aly and A. M. Abousehly, Effect of Te additions on the optical properties of (As–Sb–Se) thin films, *Thin Solid Films*, 2007, **515**(7–8), 3507–3512.

64 M. Behera, R. Naik, C. Sripan, R. Ganesan and N. C. Mishra, Influence of Bi content on linear and nonlinear optical properties of $As_{40}Se_{60-x}Bi_x$ chalcogenide thin films, *Curr. Appl. Phys.*, 2019, **19**(8), 884–893.

65 A. H. Ammar, A. M. Farid and S. S. Fouad, Optical and other physical characteristics of amorphous Ge–Se–Ag alloys, *Phys. B*, 2001, **307**(1–4), 64–71.

66 S. Das, P. Priyadarshini, D. Alagarasan, S. Vardhrajperumal, R. Ganesan and R. Naik, Role of tellurium addition on the linear and non-linear optical, structural, morphological properties of $Ag_{60-x}Se_{40}Te_x$ thin films for nonlinear applications, *J. Am. Ceram. Soc.*, 2022, **105**, 3469–3484.

67 E. R. Shaaban and I. B. I. Tomsah, The effect of Sb content on glass-forming ability, the thermal stability, and crystallization of Ge–Se chalcogenide glass, *J. Therm. Anal. Calorim.*, 2011, **105**(1), 191–198.

68 R. Naik and R. Ganesan, Effect of compositional variations on the optical properties of $Sb_xSe_{60-x}S_{40}$ thin films, *Thin Solid Films*, 2015, **579**, 95–102.

69 X. Feng, W. J. Bresser and P. Boolchand, Direct evidence for stiffness threshold in chalcogenide glasses, *Phys. Rev. Lett.*, 1997, **78**(23), 4422.